

Programmable and GPU-Accelerated Edge Inference for Real-Time ISAC on NVIDIA ARC-OTA

Davide Villa^{*†}, Mauro Belgiovine[†], Nicholas Hedberg[†],
 Michele Polese^{*}, Chris Dick[†], Tommaso Melodia^{*}

^{*}Institute for the Wireless Internet of Things, Northeastern University, Boston, MA, USA

[†]NVIDIA Corporation, Santa Clara, CA, USA

Corresponding author: villa.d@northeastern.edu

Abstract

The transition of cellular networks to (i) software-based systems on commodity hardware and (ii) platforms for services beyond connectivity introduces critical system-level challenges. As sensing emerges as a key feature toward 6G standardization, supporting Integrated Sensing and Communication (ISAC) with limited bandwidth and piggybacking on communication signals, while maintaining high reliability and performance, remains a fundamental challenge. In this paper, we provide two key contributions. First, we present a programmable, plug-and-play framework for processing PHY/MAC signals through real-time, GPU-accelerated Artificial Intelligence (AI) applications on the edge Radio Access Network (RAN) infrastructure. Building on the Open RAN dApp architecture, the framework interfaces with a GPU-accelerated gNB based on NVIDIA ARC-OTA, feeding PHY/MAC data to custom AI logic with latency under 0.5 ms for complex channel state information extraction. Second, we demonstrate the framework's capabilities through cuSense, an indoor localization dApp that consumes uplink DMRS channel estimates, removes static multipath components, and runs a neural network to infer the position of a moving person. Evaluated on a 3GPP-compliant 5G NR deployment, cuSense achieves a mean localization error of 77 cm, with 75% of predictions falling within 1 meter. This is without dedicated sensing hardware or modifications to the RAN stack or signals. We plan to release both the framework and cuSense pipelines as open source, providing a reference design for future AI-native RANs and ISAC applications.

Keywords

ISAC, dApp, 5G NR, O-RAN, CUDA-Accelerated RAN, GPU



This work is licensed under a Creative Commons Attribution-NonCommercial-ShareAlike 4.0 International License.

MobiSys '26, Cambridge, UK

© 2025 Copyright held by the owner/author(s).

ACM ISBN 978-x-xxxx-xxxx-x/YYY/MM

<https://doi.org/10.1145/nnnnnnnn.nnnnnnnn>

1 Introduction

The mobile cellular industry faces a reckoning: declining connectivity revenue and surging energy and operational costs make it harder to justify generational upgrades driven by mere connectivity gains [19]. To this end, the evolution toward sixth generation (6G) networks encompasses software stacks on generic compute accelerators, to decrease costs and make the network more flexible, *and* the identification of new revenue streams, beyond connectivity [16]. The Radio Access Network (RAN) is transforming from connectivity infrastructure to an edge platform that can provide a variety of services, leveraging the availability of rich signals and real-time telemetry at the edge, and multiplexing additional compute tasks on a programmable, accelerated infrastructure. Integrated Sensing and Communication (ISAC) represents an example in this space. Using signals available in communication stacks to enable sensing solutions has been a long-studied topic in the wireless literature [11, 25]. How to enable ISAC at scale, on top of a commercial cellular network solution, with consistent and reliable performance, limited bandwidth, and specific reference signals, remains, however, an open question. The 3rd Generation Partnership Project (3GPP) is developing ISAC study items for its Release 19 [1], toward technical specifications for 6G. Similarly, several recent papers discuss waveform design, reference-signal structures, and sensing/detection algorithms for ISAC in cellular systems, without, however, a discussion on system-level enablers [10, 26, 39].

In this paper, we address critical ISAC system challenges by demonstrating how to (i) evolve the network stack and edge RAN infrastructure to combine ISAC signal processing with Artificial Intelligence (AI) for real-time, high-accuracy sensing, while (ii) leveraging signals already defined in 5G NR specifications, captured on a standards-compliant stack using commercial smartphones. By introducing real-time, open interfaces on an open-source protocol stack accelerated on Graphics Processing Unit (GPU) and releasing a programmable ISAC framework, we establish a practical pathway to 5G-based ISAC and enable further development

in this space. Next, we discuss the challenges addressed in this paper and summarize our main contributions.

Challenge #1: Lack of Real-Time Data Exposure. RAN control and observability (e.g., with O-RAN interfaces) remain limited to near- or non-real-time scales (i.e., above 10 ms), and focused on the control plane. O-RAN programmable applications, xApps and rApps, are deployed in dedicated controllers that aggregate data from tens of Next Generation Node Bs (gNBs). They typically operate with timescales of tens of milliseconds to seconds and observe the RAN through aggregated Key Performance Indicators (KPIs), per-device and per-cell statistics computed over many slots and subcarriers. This design is intentional, as sending granular control or user-plane data—for example, I/Q samples or full Channel State Information (CSI) matrices—to a remote controller would incur prohibitive (Gbps-scale) data rates and raise security and privacy concerns. Today’s programmable RANs cannot thus leverage fine-grained PHY/Medium Access Control (MAC) telemetry for tasks that require per-slot accuracy, such as fast link adaptation, beam management, or ISAC.

Challenge #2: Real-time, High-Accuracy Estimates. Extracting accurate sensing estimates from communication signals raises both algorithmic and computational challenges. CSI is high-dimensional, noisy, and contains strong static multipath components that must be separated from the variations caused by a moving target. Thus, achieving sub-meter accuracy requires AI models capable of learning complex spatial mappings, coupled with inference pipelines that execute in real time within slot-level timing constraints, a combination that demands high computational capacity.

This work: Enabling Real-Time ISAC with GPU-accelerated dApps on the NVIDIA ARC-OTA 5G Stack. In this paper, we address these challenges by designing, implementing, and evaluating real-time GPU-accelerated ISAC, as illustrated in Figure 1. To do so, we introduce the first dApp framework for the GPU-accelerated NVIDIA Aerial RAN Co-Lab Over-the-Air (ARC-OTA) 5G-NR stack. dApps are applications co-located with the gNB that access PHY/MAC data and can directly influence RAN behavior on (sub-)millisecond timescales [13, 23, 30]. While CPU-based solutions are discussed in [23], in this paper, we design, develop, and open-source the first comprehensive dApp framework for the GPU-native NVIDIA ARC-OTA stack. This makes ARC-OTA into a platform where third-party dApps can access data on the GPU in real time and close tight control loops without compromising RAN performance, in a way that is aligned with the programmability and AI-native objectives of the O-RAN and AI-RAN Alliances.

To demonstrate the capabilities of this framework, we implement cuSense, an ISAC dApp for person tracking. cuSense consumes real-time uplink (UL) CSI estimates from the gNB and runs an AI pipeline to detect channel perturbations

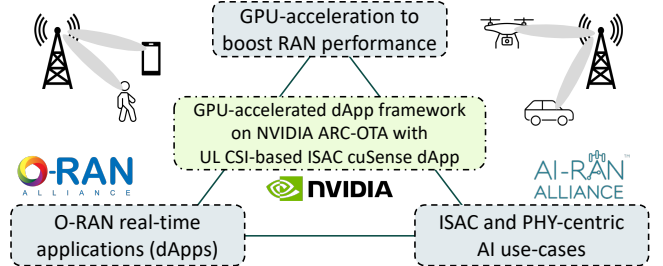


Figure 1: Overview of our work at the intersection of GPU-acceleration, O-RAN dApps, and ISAC use cases. caused by people moving and infer their two-dimensional position. We support this with an OTA data collection campaign and a labeling pipeline that combines 5G channel estimates with camera-derived ground truth, providing a concrete example of ISAC over a 3GPP-compliant RAN.

This paper makes the following contributions:

- **GPU-accelerated dApp framework.** We design a real-time dApp framework for CUDA-accelerated RANs, exposing PHY/MAC telemetry via shared-memory buffers and an E3-based control/data-plane interface.
- **Reference dApp container design.** We realize this framework on NVIDIA ARC-OTA with a modular dApp container reference architecture built around an in-gNB E3 Agent, an out-of-gNB E3 Manager, and an NVIDIA Triton-based inference pipeline that supports multiple AI backends, and we benchmark its complete E2E loop.
- **cuSense ISAC case study.** We implement cuSense, a CSI-based person-tracking dApp in an UL-collaborative ISAC setting, and define comprehensive pipelines for data collection, inference, and testing.
- **Experimental OTA evaluation and dataset.** We conduct an extensive OTA evaluation on a 3GPP-compliant RAN, characterizing latencies, overhead, and accuracy of our approach, and build a real-world OTA dataset with UL 5G CSI records and camera-based ground truth.
- **Open-source reference implementation.**¹ We provide a modular reference design and inference pipelines for dApps on a GPU-accelerated gNB and plan to release the framework, reference dApp container, and cuSense code and datasets as open source and integrated into future NVIDIA Aerial releases.

The remainder of this paper is organized as follows. Section 2 provides background and motivations for the dApp framework, which is introduced in Section 3. Section 4 evaluates the framework on ARC-OTA. Section 5 introduces cuSense, and Section 6 its evaluation. Section 7 discusses related work, and Section 8 concludes the paper.

¹The dApp framework and cuSense will be open-sourced upon acceptance of the paper.

2 dApp Background and Motivation

This section briefly reviews O-RAN and AI-native RANs, introduces dApps and prior work, and summarizes NVIDIA ARC-OTA and Aerial Data Lake (ADL) to motivate our design as illustrated in Figure 1.

AI-Native RAN Vision. Recent work in both standardization and industry is shifting towards an AI-native RAN vision, where gNBs are becoming programmable edge nodes that expose data and compute to AI workloads. The O-RAN ALLIANCE promotes this transition through a disaggregated architecture with open interfaces and RAN Intelligent Controllers (RICs) for data-driven control [34], while initiatives such as the AI-RAN Alliance further refine how AI workloads and services should be co-designed with the RAN [4].

dApps: Real-Time Distributed Applications. dApps are lightweight applications, deployed directly on the gNB, capable of accessing PHY/MAC telemetry and executing control actions at sub-10 ms timescales [13]. The architecture in [23] defines a new E3 interface to allow real-time interactions between RAN (e.g., Central Unit (CU) and Distributed Units (DUs)) and dApps, and an E3 Application Protocol (E3AP) to expose structured user-plane messages and control primitives, and demonstrates feasibility with use cases such as spectrum sharing and positioning on an OpenAirInterface (OAI)-based gNB. The O-RAN nGRG research report [30] further analyzes dApp use cases and requirements. [29] extends this line of work by embedding a GPU-accelerated dApp for UL interference detection directly into the NVIDIA Aerial pipeline. In contrast, our work introduces a generic and comprehensive GPU-driven framework that exposes a shared-memory telemetry plane and structured E3 interface to support multiple data types and models, with dApps running outside the RAN process and decoupled from custom embedded kernels.

NVIDIA ARC-OTA. NVIDIA ARC-OTA is a network stack that combines the NVIDIA Aerial in-line baseband accelerator with OAI L2 and 5G Core Network (CN) open-source stack [21], commercial Radio Units (RUs) [31]. It is designed as an AI-enabled platform for AI-RAN research, allowing developers to deploy and evaluate solutions directly on a commercial-grade, GPU-accelerated gNB. The **Aerial Data Lake** is a data capture platform that records OTA signals and associated L2 metadata from gNBs built on the Aerial stack, stores them in a database for offline post-processing [31].

2.1 Key Challenges and Requirements

Enabling dApps on a GPU platform such as ARC-OTA raises several key challenges. They motivate the design of our GPU-accelerated dApp framework, presented in Section 3.

C1: Real-time data access. dApps require low-latency access to selected data (e.g., In-phase and Quadrature (I/Q)

samples, channel estimates) without the overhead and latency of extra operations and remote RICs.

C2: Co-location with loose coupling. dApps should be co-located with the gNB to meet strict timing constraints, and also remain loosely coupled so they can be deployed and updated without modifying the production RAN.

C3: GPU-native AI tooling. The framework should be able to take advantage of the existing GPU infrastructure used by the RAN and support various AI toolchains, providing a simple path to develop and deploy new models.

C4: Isolation and scalability. Third-party dApps must be isolated from the RAN, with controlled access to shared-memory regions and compute resources, and the framework should support multiple concurrent dApps without degrading RAN performance.

C5: Alignment with standardization and existing frameworks. Interfaces and message formats should align with existing frameworks and build on E3 abstractions and serve as a reference for ongoing O-RAN, AI-RAN, and 3GPP standardization efforts on AI-native RANs and ISAC use cases.

3 GPU-accelerated dApp Framework Design

This section describes our GPU-accelerated dApp framework, including its main components and design choices.

3.1 High-Level Architecture

Figure 2 shows the architecture of an ARC-OTA gNB, extended to support our GPU-accelerated dApp framework, with three main components: (i) DU-Low running the NVIDIA Aerial CUDA L1 pipeline, ADL, and an E3 Agent component; (ii) DU-High and above running OAI open-source stack; and (iii) one or more dApps. The entire framework runs on the same physical host, requiring partitioning of host resources, such as CPU core pinning and GPU sharing mechanisms like NVIDIA Multi-Process Service (MPS) or Multi-Instance GPU (MIG), to avoid degradation of RAN performance, which remains the highest priority.

3.2 Real-Time ADL and Shared Memory

Real-time Aerial Data Lake. To satisfy *C1* (real-time data access), we extend ADL, discussed in Section 2, to a real-time version which uses a double buffering mechanism to capture and manage incoming data efficiently. As shown in Figure 3, the main thread uses two pointers ($p1$ and $p2$) that point to two buffers (*ping* and *pong*) and alternates writes between them. When one buffer is full, the thread swaps the pointers, starts collecting into the other buffer, and triggers a database insertion thread to write the completed buffer to the ClickHouse DB. The database can be configured at start time to use in-memory RAM tables or SSD storage. Since insertion is slower than capture, this ping-pong pattern

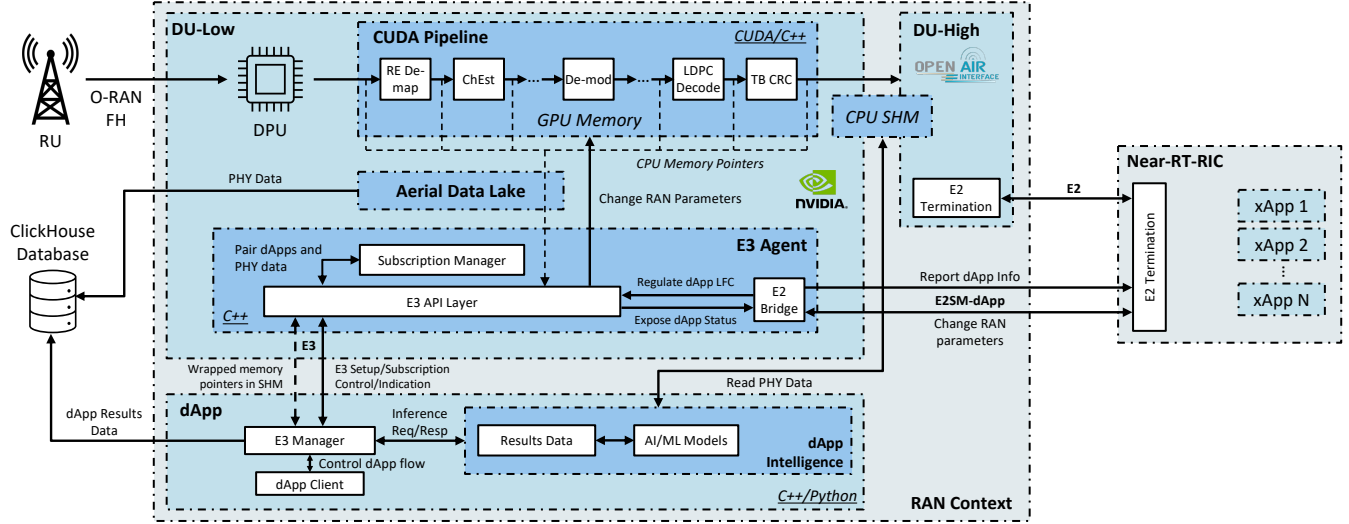


Figure 2: NVIDIA ARC-OTA dApp Integration Architecture.

allows continuous data collection without interruptions, as long as the buffers are large enough.

E3 Agent Integration. We integrate an E3 Agent into the NVIDIA Aerial software, leveraging the same initial data path pipelines, triggering mechanisms (once per uplink Transmission Time Interval (TTI)), and double-buffering abstraction of ADL. We expose the ping-pong buffers as a POSIX shared-memory object in pinned host memory with the structure shown in Figure 3, enabling direct access by external dApps. As illustrated in Figure 4, when ADL and/or the E3 Agent are enabled, the Physical Uplink Shared Channel (PUSCH) pipeline is instructed to copy (Op. 1) selected UL data from device memory (GPU) into pinned host memory via an asynchronous CUDA memcpy. This allows the CPU to proceed with other work while the GPU performs the transfers, minimizing the impact on the critical real-time L1 PHY path. Currently, we export I/Q samples, Channel Estimates (\hat{H}),

MAC Packet Data Units (PDUs), and a set of Functional Application Platform Interface (FAPI) metadata, but additional data types can be added with minimal changes.

An atomic notification (Op. 2) from the PUSCH processing then triggers the ADL routines, which write (Op. 3.1) the data from pinned host memory into the next slot of the appropriate Shared Memory (SHM) ping-pong buffer. Although these memcpy routines are fast, an additional copy is currently required to decouple data ownership between cuPHY and ADL. We plan to optimize this path by removing this extra copy in future versions, for example, by allowing the PUSCH pipeline to copy directly into SHM. If the E3 Agent is enabled, it is notified (Op. 3.2) and then packs and sends the corresponding pointers and metadata to subscribed dApps via E3 Indication messages (Op. 4). In particular, for small scalar values or metadata (e.g., slot index, cell ID), the indication carries the value directly. For larger data structures stored in SHM, the indication includes: (i) the data type (e.g., I/Q, \hat{H}); (ii) the buffer index (ping or pong); (iii) the offset

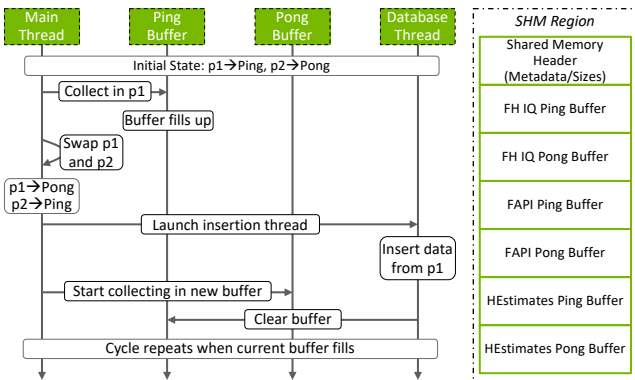


Figure 3: Aerial Data Lake ping-pong mechanism and shared memory structure.

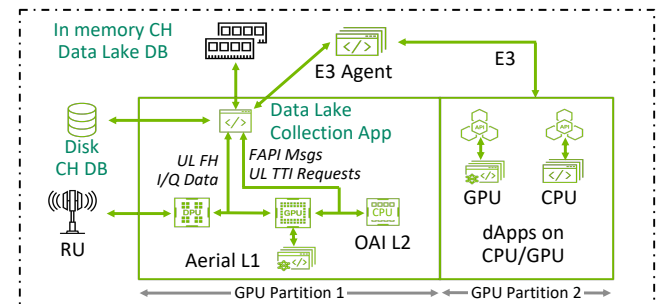


Figure 4: Data path integration between Aerial L1, Real-time ADL, shared-memory, and the E3 Agent. The steps (Op. 1–4) match the operations in Table 1.

within the buffer, expressed in units of TTIs; and (iv) optionally, the size of the written data. The dApp can then read the referenced memory while ADL and the E3 Agent prepare the next batch. Here, ADL and the E3 Agent act as read-write producers, while dApps act as read-only consumers.

Shared Memory. This pointer-based access pattern provides zero-copy data sharing between RAN and dApps, enabled by a copy path that decouples from critical GPU signal processing pipelines. Placing the buffers in host SHM also ensures portability across different deployment configurations. While NVIDIA provides direct GPU-to-GPU mechanisms, such as NVLink for peer-to-peer access and GPUDirect RDMA for inter-node communication, these require specific hardware topologies and do not support memory sharing across MIG partitions, which present isolated memory spaces even within the same physical GPU. By routing the data through pinned host memory and exposing it via SHM, our design provides a general access path for dApps regardless of whether they execute on a different MIG partition, a separate GPU, or the CPU. This also allows the same data to be accessed safely by multiple concurrent dApps while still meeting the low-latency requirements of ISAC and other sensitive applications. While the current implementation focuses on a specific set of data types, the SHM layout is generic and can be extended with additional structures by defining new regions, up to a practical limit beyond which further additions may incur performance penalties. Additionally, buffer sizes are configurable at startup, allowing for a trade-off between the amount of accessible history and memory usage. ADL and the E3 Agent share the same initial data paths and buffering mechanism, however, they can be enabled independently without changes to the RAN.

3.3 E3 Agent and E3 Manager

The E3 Agent and E3 Manager implement the communication over the recently proposed E3 interface between a RAN node and a dApp, respectively, following the E3AP procedures described in [23] of setup, subscription, indication, and control (*C5: Standardization*). As shown in Figure 5, our framework supports multiple E3 Agents running within a gNB, one for each RAN function (e.g., NVIDIA DU-Low, OAI DU-High). An E3 Manager can independently register with multiple E3 Agents and create multiple subscriptions, for example, at different sampling rates or telemetry streams. This design enables system scalability (*C4: Scalable*), allowing additional agents to be added without modifying existing dApps and for multiple dApps to subscribe to the same telemetry at different rates. Figure 5 shows two dApp examples: a spectrum sharing dApp that subscribes to L1 telemetry and sends control messages to L2 for scheduling decisions, and an ISAC dApp like cuSense that only consumes channel estimates for inference without closing the control loop.

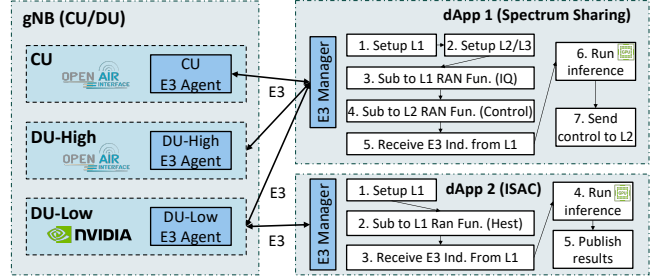


Figure 5: Support for multiple RAN nodes, E3 Agents, and dApps in the same gNB.

3.4 dApp Reference Architecture

To address *C3 (GPU-native AI tooling)* and *C4 (isolation and scalability)*, we design a reference dApp container architecture with three main components, as shown in Figure 6: (i) an E3 Manager, the required dApp orchestrator; (ii) an NVIDIA Triton Inference Server [32], our design choice for inference tasks; and (iii) a dApp Client, an optional application controller. This design serves as a concrete blueprint for deploying a GPU-accelerated dApp within a single container.

E3 Manager. The E3 Manager is a mandatory component that serves as the dApp orchestrator, interacting with the RAN nodes via the E3 interface. It manages all communication with the E3 Agent (e.g., E3 Setup and Subscription procedures) and with the dApp Client to implement the desired behavior, including application-specific Service Models (SMs). Additionally, it processes received E3 Indications by: (i) mapping the logical buffer information into the corresponding SHM locations; (ii) validating the presence and format of all inputs required by the selected AI model; (iii) preparing and sending the inference request to Triton; and (iv) post-processing the inference results for possible control actions or external reporting.

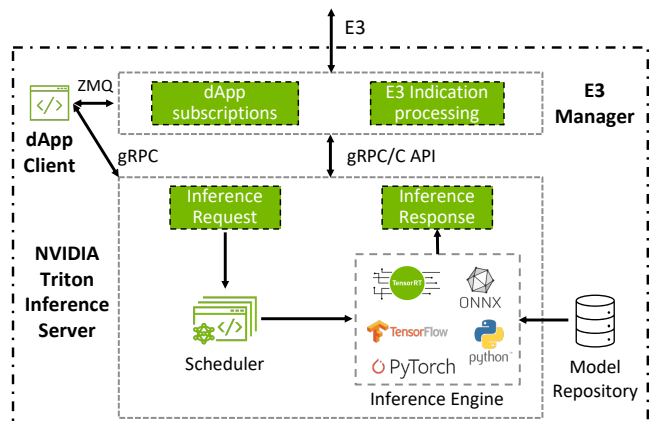


Figure 6: dApp container reference architecture with E3 Manager, NVIDIA Triton, and dApp Client.

NVIDIA Triton Inference Server. In our reference design, each dApp container hosts an instance of Triton [32], an open-source inference serving software developed by NVIDIA and optimized for GPU-accelerated inference. Developers can replace it with alternative inference engines or even lightweight Central Processing Unit (CPU)-only scripts, while still using the same dApp architecture. It exposes a model repository with models packaged as standard Triton directories and supports different backends running on CPU or GPU, including Python, PyTorch (LibTorch), Open Neural Network Exchange (ONNX) Runtime, and TensorRT (TRT). The E3 Manager and dApp client interact with Triton via its gRPC Remote Procedure Calls (gRPC)/HyperText Transfer Protocol (HTTP) or C Application Programming Interfaces (APIs) to handle model life cycles, consume memory pointers, schedule inference requests, and retrieve inference responses. Triton also allows combining different backends or running multiple models in parallel or in sequence, providing a flexible playground for benchmarking and experimentation.

dApp client. The dApp client is an optional user-level service that controls the overall dApp flow. It implements the application-specific logic by: (i) querying and managing Triton models via its gRPC APIs (e.g., selecting the model and backend to use); (ii) configuring the E3 Manager with subscription options, including the target RAN node, a list of RAN functions, Triton model to run, polling interval, duration, and SM; and (iii) performing additional post-processing of the results and triggering external events or control actions when needed. In some configurations, developers can choose to include all or part of the dApp client logic within the E3 Manager component.

This dApp design enables flexibility, as shown in Section 4, and simplifies the modular deployment of different inference pipelines, as demonstrated by the cuSense ISAC use case in Section 5. The source code will be released as open source, with documentation, guides, and inline code comments, providing developers with reference points for developing and deploying their own dApp use cases.

4 Profiling dApp Framework Performance

We now evaluate the performance of the proposed framework, integrated with NVIDIA ARC-OTA, in terms of end-to-end (E2E) control-loop latency, overhead on the RAN pipeline, and model backend flexibility. All experiments share the same ARC-OTA setup and traffic configuration, and employ either a simple reference dApp (used in this section) or the cuSense ISAC dApp described in Section 5.

4.1 ARC-OTA Experimental Setup

We perform our integration and evaluation on a standard ARC-OTA node as described in the documentation [31]. It consists of: (i) a single NVIDIA GH200 Grace Hopper (GH)

server for the RAN workloads, featuring a 72-core Grace CPU, an NVIDIA H100 Tensor Core GPU, two BlueField-3 Data Processing Units (DPUs), and two ConnectX-7 Network Interface Cards (NICs); (ii) a VIAVI Qulsar QG-2 device as grandmaster synchronization clock; (iii) an NVIDIA Spectrum-2 SN3750-SX as Front-haul (FH) switch; (iv) a 4T4R Foxconn Citizen Broadband Radio Service (CBRS) Frequency Range 1 (FR1) RU centered at 3.65 GHz with 100 MHz of bandwidth; and (v) a Samsung S23 acting as User Equipment (UE). The complete gNB stack, comprising NVIDIA Aerial L1, OAI L2 and above, the dApp framework, and OAI CN, runs within the GH200 node. The server used for the experiments presented here is not MIG-partitioned, but we have also validated the dApp framework on MIG-partitioned servers with other L2+ stacks like ORAN Development Company (ODC). CPU cores are pinned separately for L1/L2 and dApp workloads, and the GPU is shared using CUDA MPS.

4.2 Framework Benchmarks

To evaluate the performance characteristics of our framework, we conduct comprehensive benchmarking experiments measuring E2E control-loop latency and the impact of different model backends. These experiments use a simple dApp, `iq_processor`, a PHY-layer telemetry processing application that is representative of use cases such as interference detection, spectrum monitoring, and ISAC.

Reference dApp Model: `iq_processor`. Our benchmark model `iq_processor` accepts as input a tensor of I/Q samples with dimensions [4, 14, 273, 12, 2], corresponding to 4 antenna ports, 14 Orthogonal Frequency Division Multiplexing (OFDM) symbols, 273 Physical Resource Blocks (PRBs), 12 subcarriers per PRB, and 2 values (the I and Q components) in Float16 (FP16) format. This corresponds to one full UL slot of 100 MHz bandwidth data with numerology $\mu = 1$. The model computes the average power per PRB using

$$P_{\text{PRB}}(p) = \frac{1}{N_a N_s N_{sc}} \sum_{a=1}^{N_a} \sum_{s=1}^{N_s} \sum_{k=1}^{N_{sc}} (I_{a,s,p,k}^2 + Q_{a,s,p,k}^2), \quad (1)$$

where $P_{\text{PRB}}(p)$ is the average power for PRB $p \in \{1, \dots, 273\}$, $N_a = 4$ number of antennas, $N_s = 14$ the number of OFDM symbols, $N_{sc} = 12$ the number of subcarriers per PRB, and $I_{a,s,p,k}$ and $Q_{a,s,p,k}$ are the I/Q components. The output is a 273-element Float32 (FP32) vector containing the power measurements for each PRB.

End-to-end Complete Control Loop. Table 1 shows the complete control-loop data path, from the time an UL slot completes processing on the GPU pipeline, through the dApp routines, to the application of a control decision at the RAN. The communication between the E3 Agent and the E3 Manager is implemented with ZeroMQ (ZMQ), a

high-performance asynchronous messaging library for distributed systems that provides efficient request/reply and publish/subscribe socket patterns. The framework currently contributes a fixed average overhead of approximately $495\ \mu\text{s}$ plus the model-dependent inference time δ (Operation 7). Operations 1–4 ($\approx 130\ \mu\text{s}$) represent the data collection phase involving the GPU \rightarrow CPU \rightarrow SHM transfers and atomic notifications. Operations 5–8 correspond to the inference pipeline, measured as *client latency* in our backend comparison analysis. This phase includes interactions with Triton, SHM access and tensor preparation, and model inference time. For simplicity, we currently use gRPC as the communication protocol between the E3 Manager and Triton. This choice simplifies integration but dominates the overall framework overhead. We plan to replace gRPC with Triton C-based APIs to further reduce latency. Finally, Operations 9–10 close the loop by sending an optional control message back to the E3 Agent and applying it. In this benchmark, the control logic is not implemented, so the additional processing beyond ZMQ messaging is excluded.

Table 1: Data messaging path and cumulative latency for a single dApp end-to-end control-loop iteration.

| Operation | Protocol | Overhead [μs] | Total [μs] |
|--------------------------------------------|----------|----------------------------|-------------------------|
| 1. cuPHY copies data from GPU to CPU | memcpy | 35 | 35 |
| 2. cuBB notifies ADL data is ready | Atomic | 30 | 65 |
| 3. ADL copies data from CPU to SHM | memcpy | 50 | 115 |
| 4. E3 Agent sends pointers to E3 Manager | ZMQ | 15 | 130 |
| 5. E3 Manager sends request to Triton | gRPC | 150 | 280 |
| 6. Triton accesses and prepares input data | SHM | 50 | 330 |
| 7. AI Model performs inference | CUDA | δ | $330 + \delta$ |
| 8. Triton sends results to E3 Manager | gRPC | 150 | $480 + \delta$ |
| 9. E3 Manager sends control to E3 Agent | ZMQ | 15 | $495 + \delta$ |
| 10. E3 Agent receives and applies control | API | ~ 0 | $495 + \delta$ |

Note: δ represents the model-dependent inference time, which varies with model complexity and backend as shown in Figure 7.

Model Backend Performance Comparison. To assess the flexibility of the Triton-based architecture, we deploy the same iq_processor model with five different backends: (i) Python/NumPy as CPU baseline; (ii) GPU-accelerated Python using torch tensor operations; (iii) PyTorch/LibTorch with TorchScript-compiled execution; (iv) ONNX Runtime for cross-platform deployment; and (v) TRT for NVIDIA-optimized inference with FP16 precision. We benchmark these models using Triton *perf_analyzer*, a tool that generates continuous inference requests and reports both the pure mode inference time (δ) and the E2E client latency (Operations 5–8 in Table 1). The results are shown in Figure 7. The measurements highlight a substantial reduction in inference latency from more than 1 ms for the CPU baseline to just $16\ \mu\text{s}$ with the optimized TRT backend, with all GPU-based backends achieving sub-millisecond latency. On the other hand, the difference between client and inference times remains roughly constant across backends (around 440 – $480\ \mu\text{s}$),

reflecting the framework overhead due to gRPC-based communication and Triton internal request handling. Combining these client latencies with the overheads of approximately $315\ \mu\text{s}$ (Operations 1–4 and 9–10) results in full E2E control-loop latencies ranging from approximately 1.8 ms for the CPU baseline down to around $710\ \mu\text{s}$ for TRT backend. While these values are obtained from our benchmarks and may vary slightly with different dApps and subscription configurations, they provide representative reference points.

Overall, these results validate the ability of our framework to meet real-time dApp requirements, with end-to-end control-loop latencies well below 10 ms and, for GPU-accelerated backends, even below 1 ms. At the same time, it provides a flexible and performant playground for developers to experiment, prototype, and deploy a variety of applications without any architectural change.

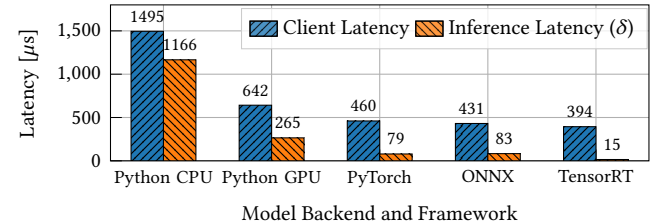


Figure 7: Client latency (Operations 5–8 of Table 1) and inference latency (δ) for the iq_processor model across different backends.

5 cuSense: Integrating ISAC in a dApp

Building upon the dApp framework presented in Section 3 and evaluated in Section 4, we now introduce cuSense, an ISAC dApp for indoor person localization using uplink CSI. This case study validates our framework’s ability to support intensive AI workloads while showcasing the potential of ISAC applications in 5G networks.

5.1 Overview and Goals

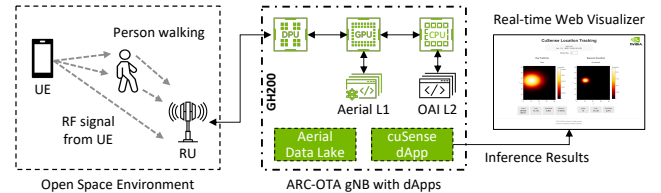


Figure 8: Overview of the cuSense UL DMRS-based ISAC dApp for person localization.

cuSense targets indoor location estimation in a single-cell CBRS deployment using CSI derived from UL PUSCH transmissions. In particular, it leverages DeModulation Reference Signal (DMRS) signals transmitted by a UE and exposed by the E3 Agent, in what is known as UL-collaborative ISAC [28].

Following the reference dApp container architecture of Section 3.4, the cuSense dApp processes these DMRSs through a lightweight signal-processing pipeline deployed in Triton, and runs a Neural Network (NN) model to capture the variations in the channel given by the moving object, as shown in Figure 8. The goal is to estimate the 2D position (x_t, y_t) of a person walking in the space through a probability map over the area of interest. The system addresses the following key challenges in UL-CSI-based sensing: (i) extracting real-time channel perturbations from static multipath; (ii) learning spatial mapping from high-dimensional CSI data; and (iii) achieving real-time inference.

Finally, cuSense is designed as a reference ISAC dApp to showcase our framework's ability to support real-time, slot-level inference, and provide a reusable dataset and base pipelines for future ISAC experiments. In the current prototype, we focus on single-user localization, but the same design can be extended without modifying the RAN to other tasks, such as occupancy monitoring and Unmanned Aerial Vehicle (UAV) or ground vehicles detection.

5.2 Uplink CSI Processing Pipeline

cuSense processes raw UL DMRS CSI measurements to estimate spatial locations of targets within an indoor environment through a three-stage pipeline: (i) background environment characterization (computed offline); (ii) temporal noise reduction and feature normalization (online in the cuSense dApp pipeline); and (iii) NN-based location estimation (online in Triton), as shown in Figure 9.

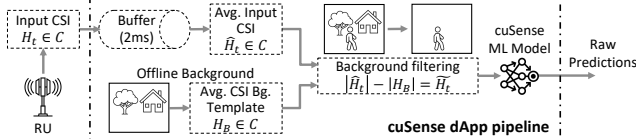


Figure 9: cuSense dApp processing pipeline overview.

Stage 1: Background Environment Characterization. The objective of this first stage is to establish a baseline characterization of the wireless channel in the absence of dynamic targets. This background template captures an averaged *snapshot* of multi-path reflections from static objects in a deployment location, such as walls, furniture, and other stationary objects, which can then be removed from live measurements to isolate target-induced perturbations.

Let $H_i[a, k, s] \in \mathbb{C}$ denote the complex CSI for measurement i at antenna a , subcarrier k , and DMRS symbol s , obtained after frequency-domain interpolation over all active subcarriers and before time-domain interpolation to all OFDM symbols. To handle variable-length subcarrier allocations with zero-padding, we define a validity set for each (a, k, s) position:

$$\mathcal{V}_{a,k,s} = \{i : |H_i[a, k, s]| > \tau\} \quad (2)$$

where $\tau = 10^{-10}$ is a tolerance power threshold, and $\mathcal{V}_{a,k,s}$ contains the indices of non-zero measurements. This ensures that statistics are computed exclusively from active subcarriers, avoiding contamination from zero-padded frequency bins that may vary across different channel allocations.

We compute a complex-valued background template by averaging over the $N_{a,k,s} = |\mathcal{V}_{a,k,s}|$ valid background measurements:

$$H_B[a, k, s] = \frac{1}{N_{a,k,s}} \sum_{i \in \mathcal{V}_{a,k,s}} H_i[a, k, s]. \quad (3)$$

The output of this stage is a complex background template H_B over active subcarriers, which is reused at inference time to remove static multi-path components.

Stage 2: Temporal Noise Reduction and Feature Normalization. This stage applies temporal averaging to mitigate measurement noise, subtracts the static background to isolate dynamic components, and normalizes features to enable stable gradient-based optimization. For each time t in a target run, we construct a causal temporal window

$$W(t) = \{H_i \mid t - \Delta t \leq t_i \leq t\}, \quad (4)$$

containing all CSI samples whose timestamp t_i falls within a window of length Δt ending at t . Based on empirical hyperparameter tuning, we set $\Delta t = 2$ ms, which provided the best trade-off between noise reduction and temporal resolution in our experiments. We then compute the phase-coherent average element-wise in the complex domain for each $W(t)$:

$$\hat{H}_t[a, k, s] = \frac{1}{|W(t)|} \sum_{i \in W(t)} H_i[a, k, s], \quad (5)$$

excluding zero-valued samples on inactive subcarriers. Temporal averaging reduces noise variance by approximately a factor of $1/|W(t)|$ under an Additive White Gaussian Noise (AWGN) assumption, improving the effective Signal-to-Noise-Ratio (SNR) while preserving the slowly varying channel characteristics associated with target motion.

To isolate dynamic components from static environment reflections, we subtract the background template in the magnitude domain from the averaged measurements,

$$\hat{H}_t[a, k, s] = |\hat{H}_t[a, k, s]| - |H_B[a, k, s]|, \quad (6)$$

and then average across the S DMRS symbols in the UL slot,

$$\tilde{H}_t^D[a, k] = \frac{1}{S} \sum_{s=1}^S \hat{H}_t[a, k, s]. \quad (7)$$

This produces a real-valued tensor $\tilde{H}_t^D \in \mathbb{R}^{A \times K_v}$, where A is the total number of receive antennas and K_v the number of active (or valid) subcarriers. This step further reduces noise through intra-slot averaging under the assumption that the channel remains approximately constant within a single OFDM slot.

Finally, we apply global z -score normalization,

$$X_t[a, k] = \frac{\tilde{H}_t^D[a, k] - \mu_{\text{global}}}{\sigma_{\text{global}} + \epsilon}, \quad (8)$$

where μ_{global} and σ_{global} are computed over all available samples, antennas, and valid subcarriers, and are then applied identically to all splits, and $\epsilon = 10^{-8}$ is a small constant to prevent division by zero. This produces standardized input features $X_t[a, k]$ for our NN model with approximately zero mean and unit variance, preserving relative power relationships between samples, which facilitates stable training and inference. In a deployed system, Stage 1 runs offline once per environment, while Stage 2 executes online inside the cuSense dApp, using the CSI data delivered by the E3 Agent via SHM.

Stage 3: Neural Network Architecture and Training.

In the last stage, we use a ResNet-inspired Convolutional Neural Network (CNN) optimized for frequency-domain, multi-antenna CSI magnitude data to predict a 2D probability grid representing the likelihood of target presence at each location within the environment. In order to account for the relatively shallow architecture and to keep the parameter count low and allow fast inference, we consider only *plain* blocks without residual connections for our architecture design (see [17] for the original model). The normalized features $X_t \in \mathbb{R}^{A \times K_v}$ are fed to our proposed architecture, as shown in Figure 10. The network consists of: (i) an initial 1D convolution and max-pooling layer; (ii) three sequential blocks with progressive channel expansion ($64 \rightarrow 128 \rightarrow 256 \rightarrow 512$); (iii) an adaptive global average pooling layer, to allow inputs of different shapes in case not all RBs are utilized in the UL transmission; (iv) a three-layer Multilayer Perceptron (MLP) stack that outputs an $H \times W$ (grid height and width) spatial probability map; and (v) a final softmax to ensure $\sum_{i,j} P_t(i, j) = 1$ for each (i, j) grid cell probability value P_t . Training uses the Kullback–Leibler (KL) divergence between the predicted distribution P_X and a smoothed target distribution P_Y as loss:

$$\mathcal{L}_{\text{KL}} = \sum_{i=0}^{H-1} \sum_{j=0}^{W-1} P_Y(i, j) \log \frac{P_Y(i, j)}{P_X(i, j)}. \quad (9)$$

This formulation encourages learning the entire spatial distribution rather than only peak locations, improving robustness to measurement noise. The target distribution is obtained by convolving a one-hot probability grid² with a 2D Gaussian kernel G_σ (label smoothing):

$$P_Y = \frac{(G_\sigma * P_{\text{one-hot}})(i, j)}{\sum_{i,j} (G_\sigma * P_{\text{one-hot}})(i, j)}, \quad (10)$$

²All grid probability values are 0, except for the target location with value equal to 1.

with $\sigma = 8.0$ in our experiments. Spatial smoothing encodes the intuition that nearby locations should receive similar probabilities, reflecting uncertainty in ground-truth annotations and measurement noise. We train the model using Adam optimizer, mini-batches of size $B = 256$, and a learning rate $l_r = 10^{-3}$ for 100 epochs. At inference time, cuSense runs Stage 2 pre-processing and the NN inside the dApp container (via Triton), receiving CSI for each UL slot t , and outputting a 2D probability map $P_t(i, j)$ over the $H \times W$ grid. From this distribution, we can derive a maximum-likelihood estimate $(\hat{i}_t, \hat{j}_t) = \arg \max_{i,j} P_t(i, j)$ to obtain the grid coordinates of highest target location probability, which can be then mapped to the relative world-coordinates. In order to reduce output predictions errors, we average the output probability for the last 10 predictions and apply Kalman filtering before returning the final estimated tracked 2D location, as detailed in Section 6.2.

6 cuSense Experimental Evaluation

To assess the feasibility and performance of cuSense, we perform an extensive OTA data-collection campaign, develop labeling pipelines to obtain ground truth and build datasets, and train and test the cuSense NN under realistic environmental conditions.

6.1 Data Collection and Labeling Methods

Measurement Campaigns. All cuSense experiments are conducted on the same ARC-OTA setup described in Section 4.1 and illustrated in Figure 11. The CBRS Foxconn RU is mounted on a custom stand [22] facing an open indoor space in NVIDIA Lab. The Samsung UE, together with a laptop used for remote access and traffic generation, is placed at the opposite end of a rectangular target area of approximately 6.78×10.06 m. We collect multiple runs under two conditions: (i) *background runs*, with no moving target present, to characterize the static channel; and (ii) *target runs*, in which a person walks along various trajectories (e.g., lawnmower, spiral, random) at normal walking speed. Each run follows the same procedure: (i) start camera recording at 30 or 60 Frames per second (FPS) (for target runs); (ii) start the ARC-OTA gNB with ADL enabled; (iii) connect the UE; (iv) start uplink UDP traffic through iperf with a target rate of 100 Mbps; (v) perform the walking trajectory within the target area (for target runs); and (vi) stop the run after approximately 2–3 minutes. Across all runs, we collect more than 400.000 CSI records together with more than 30.000 video frames, which we use in the next step for labeling and dataset construction.

Temporal Video and Sensing Synchronization. To build the complete dataset for training and testing, we collect UL CSI data (i.e., DMRS \hat{H}) together with a camera video recording the scene at a fixed frame rate, used to generate

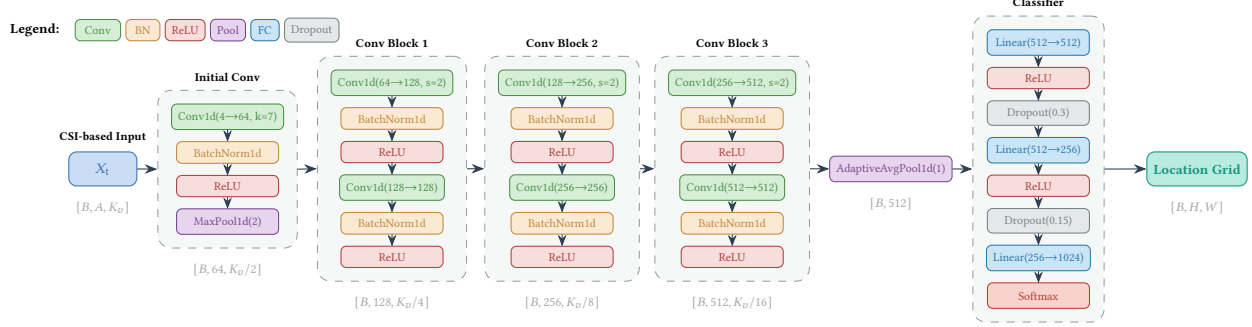


Figure 10: Proposed NN architecture of cuSense dApp for CSI-based location estimation.

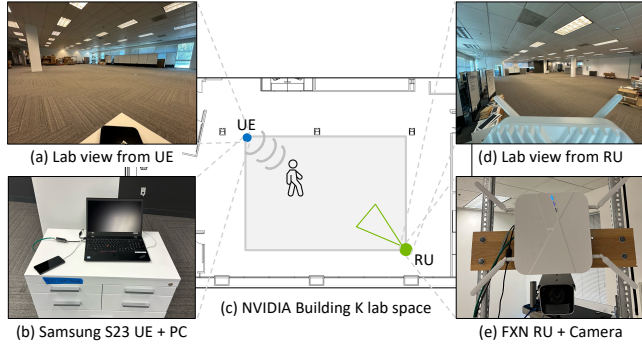


Figure 11: cuSense experimental environment.

ground-truth 2D trajectories of the person walking. Synchronizing CSI data and video frames requires handling both time-reference differences and clock skew between devices. CSI records from ADL use International Atomic Time (TAI) timestamps, while video frames from the camera (an iPhone in our experiments, though any commercial 5G camera could be used) employ standard Coordinated Universal Time (UTC) UNIX timestamps. TAI is a continuous atomic time scale that differs from UTC by a constant offset Δ_{leap} (37 s at the time of our experiments), such that $t_{\text{TAI}} = t_{\text{UTC}} + \Delta_{\text{leap}}$ due to the leap seconds introduced since 1972 to account for Earth's rotation variations. In addition to this systematic offset, we compensate for residual clock skew between the camera and the GH server with respect to a common Network Time Protocol (NTP) server. The gNB maintains microsecond-level timing accuracy through Precision Timing Protocol (PTP) synchronization with the grandmaster clock, making its contribution to skew negligible, while the camera achieves millisecond-level precision, which we estimate during the measurement campaigns. In a second step, we run an offline pipeline that parses the video file, extracts per-frame timestamps and images, and aligns them with the CSI after compensating for the 37 s TAI offset and the measured server–camera clock skew. We assign each CSI record to the closest video frame within a threshold of half the frame period, generating tightly synchronized CSI-video pairs, where a single frame may correspond to multiple CSI records.

Ground-Truth Extraction. To extract the ground-truth locations, we derive the 2D person coordinates from the camera stream using an offline computer-vision pipeline based on YOLOv8 [20]. For each video frame, we run a person detector and retain the bounding box with the highest confidence (our experiments are limited to a single walking subject). The box centroid (u, v) in image coordinates is then projected onto the floor plane using a planar homography H estimated from the manually annotated image corners of the rectangular area of interest in the environment. This generates a continuous trajectory $\{(x_t, y_t)\}$ in meters, sampled at the camera frame rate. Each CSI record then inherits a physical position (x_t, y_t) , since it is associated with the closest video frame in time. For training, we discretize the floor plan into an $H \times W$ grid and quantize each position to the corresponding cell (i, j) , producing a one-hot label $P_{\text{one-hot}}(i, j)$ for that CSI sample. These one-hot labels are then converted into smoothed target distributions P_{target} using the Gaussian label-smoothing procedure described in Stage 3.

6.2 Performance Results

We now evaluate cuSense on the dataset described in Section 6.1, focusing on three aspects: (i) localization accuracy against the ground-truth; (ii) comparison with 3GPP sensing service categories; and (iii) real-time inference capability within our dApp framework.

Dataset and Evaluation Setup. The cuSense model is trained on CSI data from 5 runs with a moving target, for a total of 362,318 slot samples each with 4 antennas and 3 DMRS symbols. We use a temporal-random split strategy of 80% training, 10% validation, 10% test as shown in the examples of Figure 12. Validation and test sets are two contiguous temporal blocks randomly positioned within each run's timeline, rather than randomly sampling individual points. This design choice is critical because consecutive CSI values may be highly correlated, leading to overfitting and poor generalization to unseen trajectories. The background template H_B is computed from a single dedicated run of 54,400 samples in a static environment with no moving target. We also evaluate

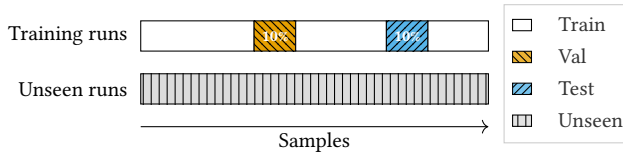


Figure 12: Temporal-random split strategy with example of contiguous validation/test blocks within training runs and fully unseen runs.

cuSense generalization across two independent unseen runs (Unseen-Run 1 and Unseen-Run 2) collected separately from all training, testing, or validation data. We measure localization performance using standard Root Mean Squared Error (RMSE), median, and success rate within different thresholds over all unseen CSI records. Additionally, the inference pipeline applies a temporal arithmetic mean over 10 consecutive predictions from stage 3 processing output for noise reduction, followed by a Kalman filter tracking with process noise $Q = 10^{-5}$ and measurement noise base $R_{\text{base}} = 750$ to produce temporally coherent trajectory estimates.

Localization Accuracy. Table 2 summarizes the localization performance on the unseen runs. cuSense achieves a mean localization error of 77.4 cm with a median of 58.7 cm, demonstrating sub-meter accuracy for the majority of predictions. The RMSE of 103 cm reflects occasional outliers in challenging multipath conditions. Notably, performance is consistent across both test campaigns (75.1 and 79.7 cm), indicating robust generalization to unseen measurement campaigns in the same environment.

Table 2: cuSense localization accuracy on unseen runs.

| Metric | Unseen-Run 1 | Unseen-Run 2 | Average |
|-------------------|--------------|--------------|---------|
| Samples | 47,211 | 47,404 | - |
| Mean Error [cm] | 75.1 | 79.7 | 77.4 |
| Median Error [cm] | 54.9 | 62.6 | 58.7 |
| Std. Dev. [cm] | 67.6 | 68.3 | 68.0 |
| RMSE [cm] | 101.0 | 105.0 | 103.0 |

3GPP Sensing Service Categories. We benchmark these results against the 3GPP Release 19 sensing accuracy categories defined for 5G wireless sensing applications [1]. Figures 13a and 13b show the cumulative accuracy at each category threshold, and the error Cumulative Distribution Function (CDF) for the test set (approximately 35k samples from the temporal-random split of training), while Figures 13c and 13d present the same metrics for the two completely unseen runs (over 94k samples). On the test set, around 42% of predictions achieve Category 4 accuracy (≤ 50 cm), with cumulative sub-meter accuracy of 75% (Categories 4 and 3). We note that performance on unseen runs remains consistent with 43% of predictions falling within Category 4 and over 74% within Category 3, despite these runs being entirely excluded from training. This indicates that the model

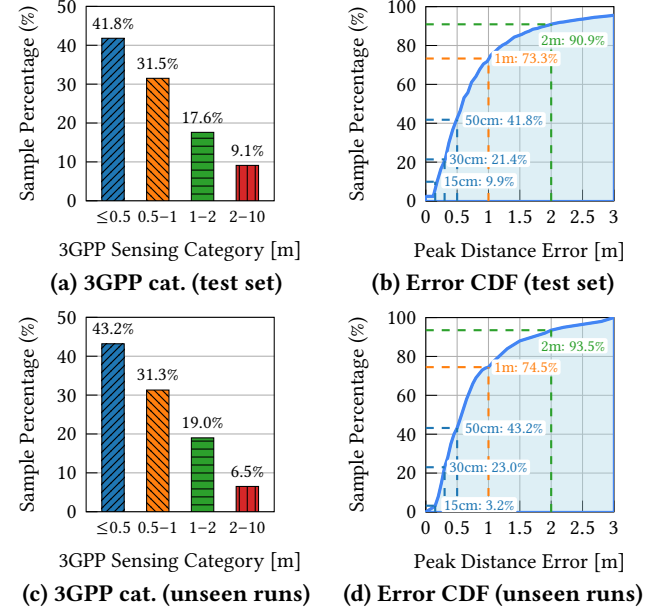


Figure 13: cuSense localization accuracy on test set (a, b) and unseen runs (c, d): 3GPP wireless sensing service category distributions and CDF of peak distance error.

generalizes well to new trajectories within the same environment rather than overfitting to training data. Over 93% of predictions meet Category 2 requirements (≤ 2 m) for the unseen runs, with the remaining predictions within Category 1 (2–10 m). These results demonstrate that cuSense meets 3GPP sensing requirements for indoor localization applications such as asset tracking, occupancy monitoring, and intelligent building automation.

Trajectory Tracking. Figure 14 visualizes the X and Y position estimates over time for a representative test segment (downsampled to 10 for clarity), comparing raw model predictions, temporally averaged predictions, Kalman-filtered output, and ground truth. The raw predictions exhibit significant frame-to-frame jitter from measurement noise. Tem-

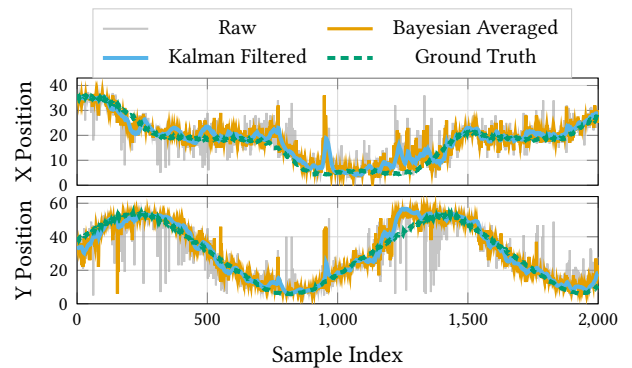


Figure 14: Trajectory tracking comparison of an unseen run segment for the X and Y axis.

poral averaging reduces this variability, while the Kalman filter produces smooth, physically plausible trajectories that closely track the ground truth. The multi-stage refinement provides cumulative error reduction of 30–40% compared to raw predictions, with the Kalman filter successfully handling both slow movements and rapid direction changes.

Real-Time dApp Inference Performance. Table 3 shows the computational performance of the cuSense dApp inference pipeline. The complete pipeline—including CSI pre-processing (background removal and temporal averaging), NN inference via Triton, prediction averaging, and Kalman filtering—achieves a mean E2E latency of 1.36 ms per sample with PyTorch, and 0.65 ms with TRT acceleration. Combined with the dApp framework overhead of 495 μ s (Table 1), the total cuSense control-loop latency is approximately 1.85 ms (or 1.15 ms with TRT), well within real-time requirements for tracking applications.

Table 3: cuSense inference latency breakdown.

| Operation | Overhead [ms] |
|-----------------------------|-----------------------------|
| CSI preprocessing | 0.3 |
| Neural network inference | 0.8 (PyTorch) - 0.1 (TRT) |
| Bayesian temporal averaging | 0.1 |
| Kalman filter tracking | 0.15 |
| Total inference Latency | 1.35 (PyTorch) - 0.65 (TRT) |

7 Related Work

Open and AI-Native RAN Testbeds. Several open and AI-native 5G/O-RAN testbeds have been proposed to accelerate experimentation with data-driven RAN control. [36] provides an open-source O-RAN platform with non-RT, near-RT, and a proposed real-time RIC (zApps) for AI-based RAN management. [14] introduces a digital-twin-based AI-RAN development workflow and an NVIDIA ARC-OTA-based testbed for AI PHY evaluation with commercial UEs. Other platforms such as POWDER, COSMOS, Colosseum, and X5G enable at-scale experimentation with open RAN and GPU-accelerated PHY functions [5, 7, 8, 37]. Our work builds on this ecosystem and focuses on integrating dApps with ARC-OTA and exposing on-GPU PHY/MAC telemetry for real-time applications, such as spectrum sharing and ISAC.

dApps and Real-Time Programmability. Recent work extends O-RAN toward real-time and user-plane control following initial visions and implementations (see Section 2) [13, 23, 30]. Follow-up work demonstrates dApps for CPU power management, spectrum classification, and interference detection on GPU-accelerated 5G PHYs [9, 29, 33]. Janus takes a complementary approach, embedding eBPF-based “codelets” directly into vRAN functions to enable flexible telemetry and real-time control with strict safety guarantees [15], while [36] zApps target similar real-time functionality below the

10 ms timescale at the RIC level. Compared to these systems, our work focuses on PHY telemetry on GPU on a production-grade ARC-OTA deployment and uses dApps to implement intelligent GPU-accelerated applications by creating complete E2E pipelines for generic real-time data access and consumption, while keeping dApps outside the gNB process and decoupled from vendor-specific PHY kernels.

ISAC and CSI-based Sensing. ISAC has been widely studied as a key enabler for beyond-5G and 6G networks, with recent surveys reviewing system architectures, performance limits, and open challenges [24, 27]. In the context of 5G, recent work has explored communication-centric ISAC schemes for cooperative target localization and UL-collaborative sensing using OFDM/NR signals [18, 40], as well as passive radar sensing and CSI-based localization using NR reference signals [6, 12, 35]. Earlier Wi-Fi sensing systems [2, 3, 38] have demonstrated that commodity Wi-Fi signals and CSI can enable fine-grained localization and person perception. Our work is complementary to this literature: rather than using Wi-Fi or standalone receivers, we implement CSI-based indoor localization as an uplink-collaborative ISAC service directly on a 3GPP-compliant, GPU-accelerated 5G gNB, exposing it as a programmable dApp within an O-RAN/AI-RAN framework without dedicated sensing hardware or changes to the RAN stack.

8 Conclusions and Future Work

In this work, we designed, implemented, and evaluated a GPU-accelerated framework for real-time O-RAN dApps on NVIDIA ARC-OTA that exposes PHY/MAC telemetry via SHM and an E3-based interface, enabling E2E control loops with less than 500 μ s overhead. On top of this framework, we realized cuSense, an uplink DMRS CSI-based indoor localization dApp operating in real time on a production-grade 5G network without dedicated sensing hardware or RAN modifications. Experiments across independent unseen runs show sub-meter accuracy and consistent performance, indicating robust generalization within the same environment.

The current UL-collaborative bistatic architecture with a transmitting UE offers a practical deployment model but also limits spatial diversity and relies on environment-specific calibration and the availability of collaborative devices. These constraints motivate future work on dynamic environments, multi-cell configurations, multi-targets, and sensing modes that reduce or eliminate the need for explicit collaboration. Going forward, we plan to release the dApp framework and cuSense as open-source components, providing the community with a reference design, pipelines, and datasets to enable and advance the development of GPU-accelerated real-time applications for AI-native RAN.

References

[1] 3GPP. 2024. *Study on Integrated Sensing and Communication*. Technical Specification 22.137. 3rd Generation Partnership Project (3GPP). https://www.3gpp.org/ftp/Specs/archive/22_series/22.137/

[2] Fadel Adib, Zach Kabelac, Dina Katabi, and Robert C. Miller. 2014. 3D Tracking via Body Radio Reflections. In *11th USENIX Symposium on Networked Systems Design and Implementation (NSDI 14)*. USENIX Association, Seattle, WA, 317–329.

[3] Fadel Adib and Dina Katabi. 2013. See through walls with WiFi! *SIGCOMM Comput. Commun. Rev.* 43, 4 (August 2013), 75–86.

[4] AI-RAN Alliance. 2024. AI-RAN Alliance: Vision and Mission White Paper. https://ai-ran.org/wp-content/uploads/2024/12/AI-RAN_Alliance_Whitepaper.pdf

[5] Leonardo Bonati, Pedram Johari, Michele Polese, Salvatore D’Oro, Subhramoy Mohanti, Miead Tehrani-Moayyed, Davide Villa, Shweta Shrivastava, Chinene Tassie, Kurt Yoder, Ajeet Bagga, Paresh Patel, Ventz Petkov, Michael Seltser, Francesco Restuccia, Abhimanyu Gosain, Kaushik R. Chowdhury, Stefano Basagni, and Tommaso Melodia. 2021. Colosseum: Large-Scale Wireless Experimentation Through Hardware-in-the-Loop Network Emulation. In *Proceedings of IEEE Intl. Symp. on Dynamic Spectrum Access Networks (DySPAN)*. Virtual Conference.

[6] Nada Boukanna, Mohsen Ahadi, Florian Kaltenberger, and Robert Schmidt. 2025. An O-RAN Framework for AI/ML-Based Localization with OpenAirInterface and FlexRIC. *arXiv:2511.19233 [cs.NI]*

[7] Joe Breen, Andrew Buffmire, Jonathon Duerig, Kevin Dutt, Eric Eide, Mike Hibler, David Johnson, Sneha Kumar Kasera, Earl Lewis, Dustin Maas, Alex Orange, Neal Patwari, Daniel Reading, Robert Ricci, David Schurig, Leigh B. Stoller, Jacobus Van der Merwe, Kirk Webb, and Gary Wong. 2020. POWDER: Platform for Open Wireless Data-driven Experimental Research. In *Proceedings of ACM WiNTECH* (London, United Kingdom). New York, NY, USA.

[8] Tingjun Chen, Prasanthi Maddala, Panagiotis Skrimponis, Jakub Kolodziejksi, Abhishek Adhikari, Hang Hu, Zhihui Gao, Arun Paidimari, Alberto Valdes-Garcia, Myung Lee, Sundeep Rangan, Gil Zussman, and Ivan Seskar. 2023. Open-access millimeter-wave software-defined radios in the PAWR COSMOS testbed: Design, deployment, and experimentation. *Computer Networks* 234 (October 2023), 109922.

[9] Francisco Crespo, Javier Villegas, Carlos Baena, Eduardo Baena, Sergio Fortes, and Raquel Barco. 2025. Energy-Aware CPU Orchestration in O-RAN: A dApp-Driven Lightweight Approach. *arXiv:2508.00629 [cs.NI]*

[10] Yuanhao Cui, Xiaojun Jing, and Junsheng Mu. 2022. Integrated Sensing and Communications Via 5G NR Waveform: Performance Analysis. In *ICASSP 2022 - 2022 IEEE International Conference on Acoustics, Speech and Signal Processing (ICASSP)*. 8747–8751.

[11] Yuanhao Cui, Fan Liu, Xiaojun Jing, and Junsheng Mu. 2021. Integrating Sensing and Communications for Ubiquitous IoT: Applications, Trends, and Challenges. *IEEE Network* 35, 5 (2021), 158–167.

[12] Manu Dwivedi, Ian Ellis L. Hulede, Oscar Venegas, Jonathan Ashdown, and Amitav Mukherjee. 2024. 5G-Based Passive Radar Sensing for Human Activity Recognition Using Deep Learning. In *2024 IEEE Radar Conference (RadarConf24)*. 1–6.

[13] Salvatore D’Oro, Michele Polese, Leonardo Bonati, Hai Cheng, and Tommaso Melodia. 2022. dApps: Distributed Applications for Real-Time Inference and Control in O-RAN. *IEEE Communications Magazine* 60, 11 (Nov. 2022), 52–58.

[14] Russell Ford, Hao Chen, Pranav Madadi, Mandar Kulkarni, Xiaochuan Ma, Daoud Burghal, Guanbo Chen, Yeqing Hu, Chance Tarver, Panagiotis Skrimponis, Vitali Loseu, Yu Zhang, Yan Xin, Yang Li, Jianzhong Zhang, Shubham Khunteta, Yeswanth Gudetti Reddy, Ashok Kumar Reddy Chavva, Mahantesh Kothiwale, and Davide Villa. 2025. Sim2Field: End-to-End Development of AI RANs for 6G. In *Proceedings of ACM Workshop on Open and AI RAN*. Hong Kong, China.

[15] Xenofon Foukas, Bozidar Radunovic, Matthew Balkwill, and Zhihua Lai. 2023. Taking 5G RAN Analytics and Control to a New Level. In *Proceedings of ACM MobiCom ’23* (Madrid, Spain). ACM, New York, NY, USA.

[16] Marco Giordani, Michele Polese, Marco Mezzavilla, Sundeep Rangan, and Michele Zorzi. 2020. Toward 6G Networks: Use Cases and Technologies. *IEEE Communications Magazine* 58, 3 (2020), 55–61.

[17] Kaiming He, Xiangyu Zhang, Shaoqing Ren, and Jian Sun. 2016. Deep Residual Learning for Image Recognition. In *Proceedings of the IEEE Conference on Computer Vision and Pattern Recognition (CVPR)*.

[18] Peiwei Huang, Fan Liu, Fuwang Dong, and Zhenkun Wang. 2025. Uplink Collaborative Sensing with OFDM Communication Signals. In *ICC 2025 - IEEE International Conference on Communications*. 1–6.

[19] Wei Jiang, Bin Han, Mohammad Asif Habibi, and Hans Dieter Schotten. 2021. The Road Towards 6G: A Comprehensive Survey. *IEEE Open Journal of the Communications Society* 2 (2021), 334–366.

[20] Glenn Jocher, Jing Qiu, and Ayush Chaurasia. 2023. Ultralytics YOLO. <https://github.com/ultralytics/ultralytics>

[21] Florian Kaltenberger, Tommaso Melodia, Irfan Ghauri, Michele Polese, Raymond Knopp, Tien Thinh Nguyen, Sakthivel Velumani, Davide Villa, Leonardo Bonati, Robert Schmidt, Sagar Arora, Mikel Izazabal, and Navid Nikaein. 2025. Driving Innovation in 6G Wireless Technologies: The OpenAirInterface Approach. *Computer Networks* 269 (September 2025), 111410.

[22] Anupa Kelkar and Chris Dick. 2021. NVIDIA Aerial GPU Hosted AI-on-5G. In *2021 IEEE 4th 5G World Forum (5GWF)*. 64–69.

[23] Andrea Lacava, Leonardo Bonati, Niloofar Mohamadi, Rajeev Ganguly, Florian Kaltenberger, Pedram Johari, Salvatore D’Oro, Francesca Cuomo, Michele Polese, and Tommaso Melodia. 2025. dApps: Enabling Real-Time AI-Based Open RAN Control. *Computer Networks* 269 (September 2025), 111342.

[24] An Liu, Zhe Huang, Min Li, Yubo Wan, Wenrui Li, Tony Xiao Han, Chenchen Liu, Rui Du, Danny Kai Pin Tan, Jianmin Lu, Yuan Shen, Fabiola Colone, and Kevin Chetty. 2022. A Survey on Fundamental Limits of Integrated Sensing and Communication. *IEEE Communications Surveys & Tutorials* 24, 2 (February 2022), 994–1034.

[25] Fan Liu, Yuanhao Cui, Christos Masouros, Jie Xu, Tony Xiao Han, Yonina C. Eldar, and Stefano Buzzi. 2022. Integrated Sensing and Communications: Toward Dual-Functional Wireless Networks for 6G and Beyond. *IEEE Journal on Selected Areas in Communications* 40, 6 (2022), 1728–1767.

[26] Ruiqi Liu, Mengnan Jian, Dawei Chen, Xu Lin, Yichao Cheng, Wei Cheng, and Shijun Chen. 2023. Integrated sensing and communication based outdoor multi-target detection, tracking, and localization in practical 5G Networks. *Intelligent and Converged Networks* 4, 3 (2023), 261–272.

[27] Shihang Lu, Fan Liu, Yunxin Li, Kecheng Zhang, Hongjia Huang, Jiaqi Zou, Xinyu Li, Yuxiang Dong, Fuwang Dong, Jia Zhu, Yifeng Xiong, Weijie Yuan, Yuanhao Cui, and Lajos Hanzo. 2024. Integrated Sensing and Communications: Recent Advances and Ten Open Challenges. *IEEE Internet of Things Journal* 11, 11 (June 2024), 19094–19120.

[28] Kaitao Meng, Christos Masouros, Athina P. Petropulu, and Lajos Hanzo. 2025. Cooperative ISAC Networks: Opportunities and Challenges. *IEEE Wireless Communications* 32, 3 (June 2025), 212–219.

[29] N. Neasamoni Santhi, Davide Villa, Michele Polese, and Tommaso Melodia. 2025. InterfO-RAN: Real-Time In-band Cellular Uplink Interference Detection with GPU-Accelerated dApps. *Proc. of ACM International Symposium on Theory, Algorithmic Foundations, and Protocol Design for Mobile Networks and Mobile Computing (MobiHoc)* (October 2025).

- [30] Northeastern University, NVIDIA, Mavenir, MITRE, and Qualcomm. 2024. dApps for Real-Time RAN Control: Use Cases and Requirement. <https://mediastorage.o-ran.org/ngrrg-rr/nGRG-RR-2024-10-dApp%20use%20cases%20and%20requirements.pdf>
- [31] NVIDIA. 2025. Aerial RAN co-lab over-the-air (ARC-OTA). <https://docs.nvidia.com/aerial/aerial-ran-colab-ota/current/index.html>
- [32] NVIDIA Corporation. 2018. Triton Inference Server: An Optimized Cloud and Edge Inferencing Solution. <https://docs.nvidia.com/deeplearning/triton-inference-server/user-guide/docs/index.html> Accessed December 2025.
- [33] Filippo Olimpieri, Noemi Giustini, Andrea Lacava, Salvatore D’Oro, Tommaso Melodia, and Francesca Cuomo. 2025. LibIQ: Toward Real-Time Spectrum Classification in O-RAN dApps. In *Proceedings of IEEE Mediterranean Communication and Computer Networking Conference (MedComNet)* (Cagliari, Italy).
- [34] Michele Polese, Leonardo Bonati, Salvatore D’Oro, Stefano Basagni, and Tommaso Melodia. 2023. Understanding O-RAN: Architecture, Interfaces, Algorithms, Security, and Research Challenges. *IEEE Communications Surveys & Tutorials* 25, 2 (Q2 2023), 1376–1411.
- [35] Yanlin Ruan, Liang Chen, Xin Zhou, Guangyi Guo, and Ruizhi Chen. 2022. Hi-Loc: Hybrid Indoor Localization via Enhanced 5G NR CSI. *IEEE Transactions on Instrumentation and Measurement* 71 (August 2022), 1–15.
- [36] Pratheek S. Upadhyaya, Nishith Tripathi, Joseph Gaeddert, and Jeffrey H. Reed. 2023. Open AI Cellular (OAIC): An Open Source 5G O-RAN Testbed for Design and Testing of AI-Based RAN Management Algorithms. *IEEE Network* 37, 5 (September 2023), 7–15.
- [37] Davide Villa, Imran Khan, Florian Kaltenberger, Nicholas Hedberg, Rúben Soares da Silva, Stefano Maxenti, Leonardo Bonati, Anupa Kelkar, Chris Dick, Eduardo Baena, Josep M. Jornet, Tommaso Melodia, Michele Polese, and Dimitrios Koutsonikolas. 2025. X5G: An Open, Programmable, Multi-Vendor, End-to-End, Private 5G O-RAN Testbed With NVIDIA ARC and OpenAirInterface. *IEEE Transactions on Mobile Computing* 24, 11 (2025), 11305–11322.
- [38] Fei Wang, Sanping Zhou, Stanislav Panev, Jinsong Han, and Dong Huang. 2019. Person-in-WiFi: Fine-Grained Person Perception Using WiFi. In *Proceedings of the IEEE/CVF International Conference on Computer Vision (ICCV)*.
- [39] Zhiqing Wei, Fengyun Li, Haotian Liu, Xu Chen, Huici Wu, Kaifeng Han, and Zhiyong Feng. 2024. Multiple Reference Signals Collaborative Sensing for Integrated Sensing and Communication System Towards 5G-A and 6G. *IEEE Transactions on Vehicular Technology* 73, 10 (2024).
- [40] Zhenkun Zhang, Hong Ren, Cunhua Pan, Sheng Hong, Dongming Wang, Jiangzhou Wang, and Xiaohu You. 2025. Target Localization in Cooperative ISAC Systems: A Scheme Based on 5G NR OFDM Signals. *IEEE Transactions on Communications* 73, 5 (May 2025), 3562–3578.